Supplementary Materials:

Preparation of Mg-5wt%Ca-1wt%Zn Alloy

Mg-5wt%Ca-1wt%Zn alloy was prepared using commercially available pure Mg (99.98%) ingots, Ca (99.99%) metal grains, and Zn (99.99%) metal grains in a vacuum furnace. The high purity argon gas was applied (99.999%) after atmosphere of the furnace was purged to 5 $\times 10^{-2}$ torr. The melt was cast into a STS430 steel mold at melting temperature of 750°C. The as-cast ingots were preheated to ~350°C and then extruded into rods with an extrusion ratio of 39:1, after which the samples were cooled in air. The inductively coupled plasma (ICP, ARIAN 710-ES) method was used to analyze the chemical compositions of the alloy. The precise and complete alloy composition including trace elements responsible for accelerated corrosion is as followed.

	Composition of the extruded Mg-5wt%Ca-1wt%Zn alloys analyzed by ICP method						
Elements	Ca	Zn	Mn	Fe	Ni	Si	B
wt%	5.12	1.17	<0.001	<0.002	<0.002	<0.001	<0.002

Table S1. Composition of the extruded Mg-5wt%Ca-1wt%Zn Alloy analyzed by ICP method

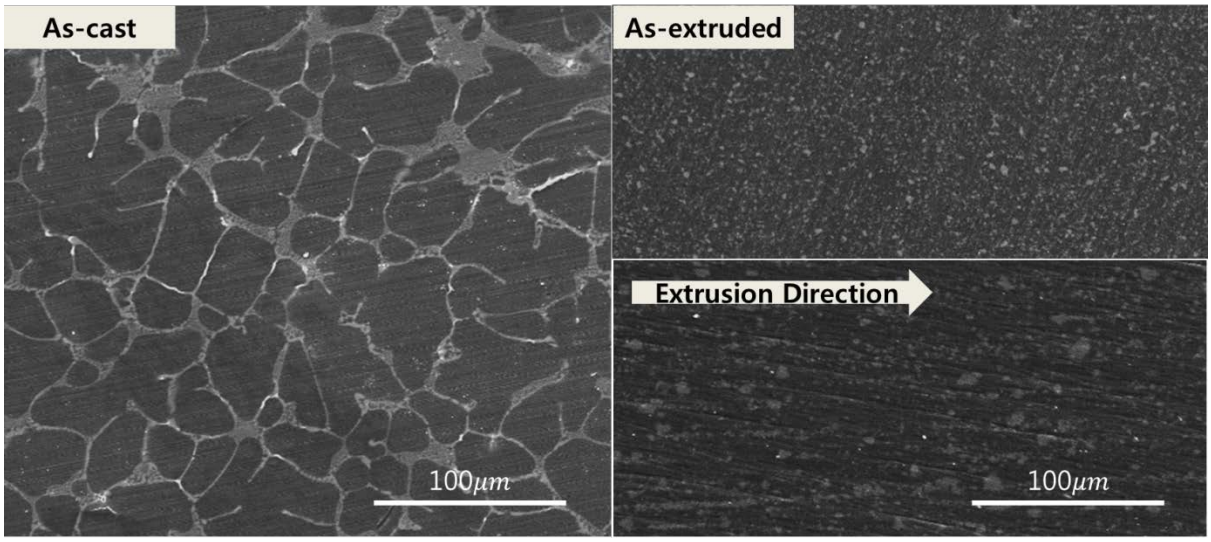

Fig. S1. microstructure of as-cast Mg-5wt%Ca-1wt%Zn alloy and as-extruded alloy with the extrusion direction

Note) Extrusion of Mg-5wt%Ca-1wt%Zn alloy reduced the grain size to ~10 μm. Effective grain refinement of the ternary alloy was induced by the particle pinning effect of the second phase and caused larger drop of its corrosion rate compared to high purity Mg. Below image shows the microstructure of as-cast Mg-5wt%Ca-1wt%Zn alloy and as-extruded alloy with the extrusion direction.

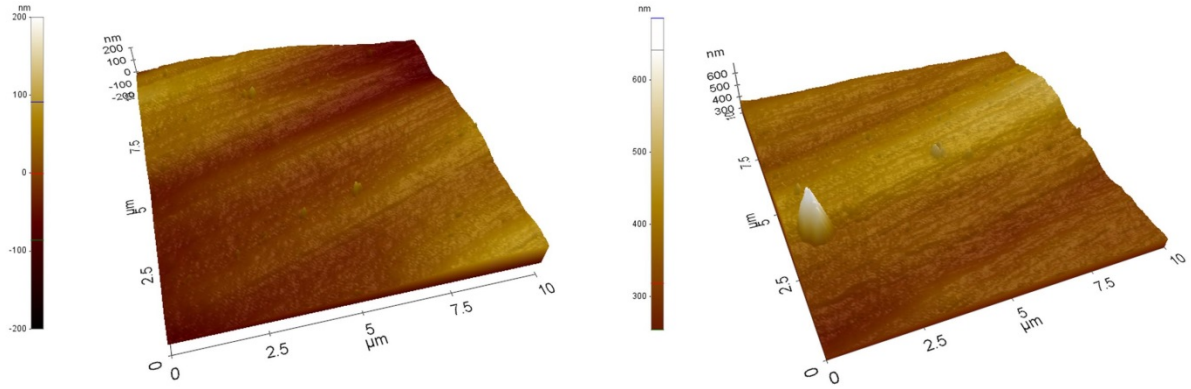

Fig. S2. AFM images of Mg samples. AFM images of independently prepared Mg substrates with a detection area of 100 μm^2.

Note) In order to measure the surface roughness, we performed atomic-force-microscopy (AFM) analysis of the samples with a detection area of 100 μm^2. For the Mg billets, two independently prepared samples were analyzed, and the roughness value of each sample was similar: approximately 22.4 nm.

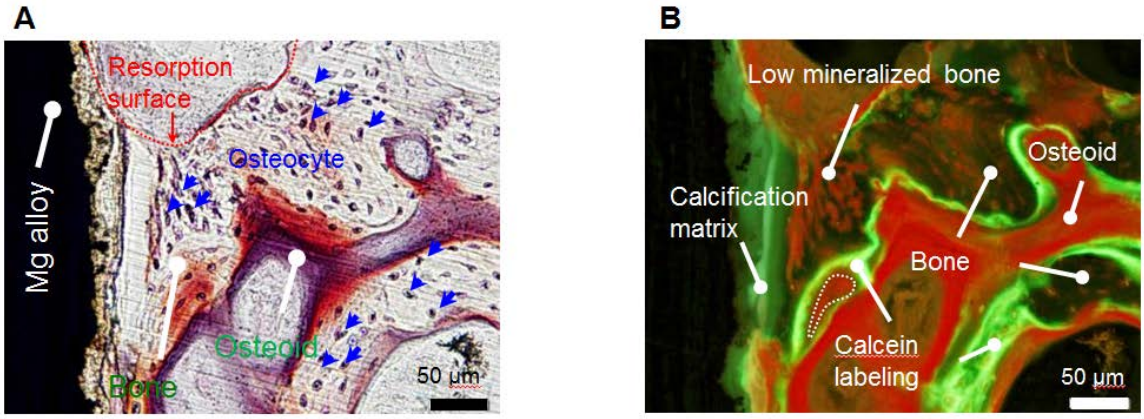

Fig. S3. Characteristics of Villanueva staining.

(A) Under natural light, observation of bone tissues and cellular tissues such as osteoclasts, osteoblasts, osteocytes, and osteoids (appear in purple color) are made possible. Furthermore, bone resorption surface and cement lines are also visible. (B) Under the fluorescent light, calcein labelings can be observed and calcification matrix, bone, osteoid appears in fluorescent, dark green, and red, respectively.

Note) Simultaneous observation of Villanueva stained slides under two different set of light source allowed histological observation of acellular matrix, which is a unique degradation product from Mg alloy implant. Acellular matrix is not visible when conventional bone histological methods such as Von Kossa, toluidine blue, and Goldner's trichrome staining are used (1).

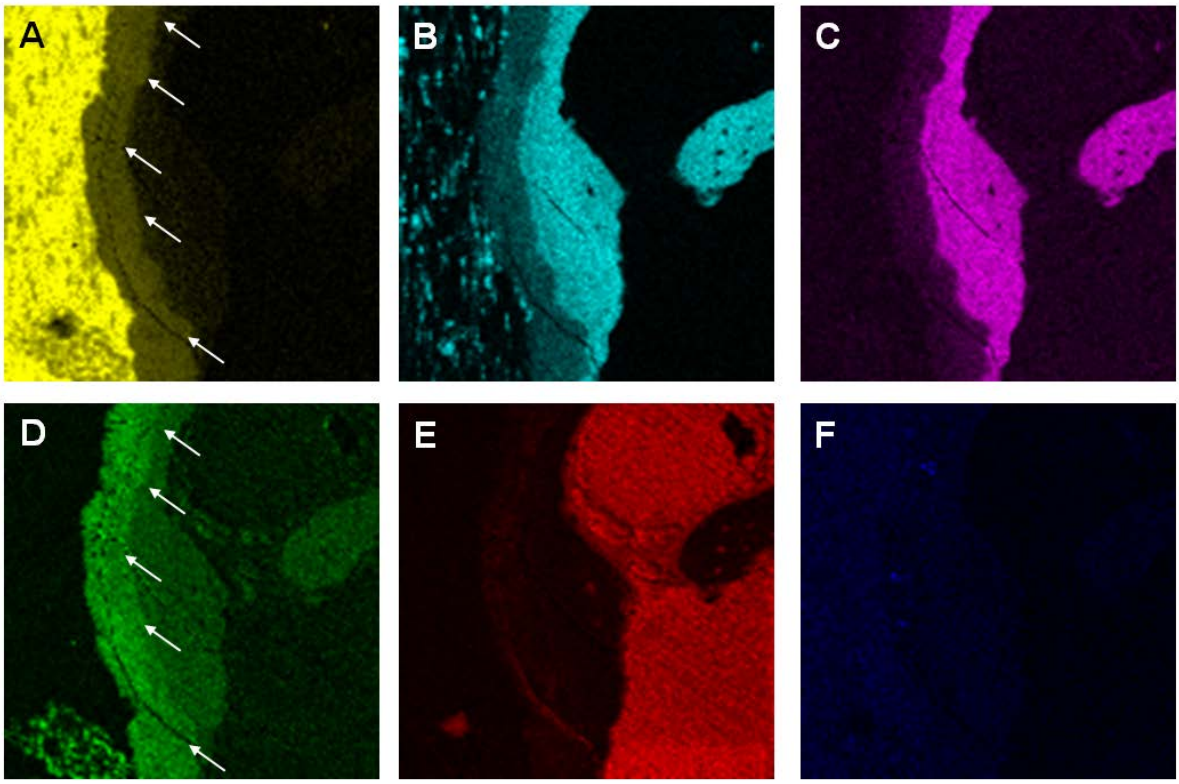

Fig. S4. SEM/EDX mapping of Mg alloy implant interface areas shown in Fig. 1. Results from EDX Mapping of (A) Mg, (B) Ca, (C) P, (D) O, (E) C, and (F) Zn. Bone area and calcification matrix area cannot be distinguished from each other and are mainly composed of large amount of Ca and P and a small amount of O. Layer with large amount of O (d; indicated by arrows) contains little amount of Mg (a; indicated by arrows), Ca and P, which suggests well-known Mg and O rich compound $Mg(OH)_2$.

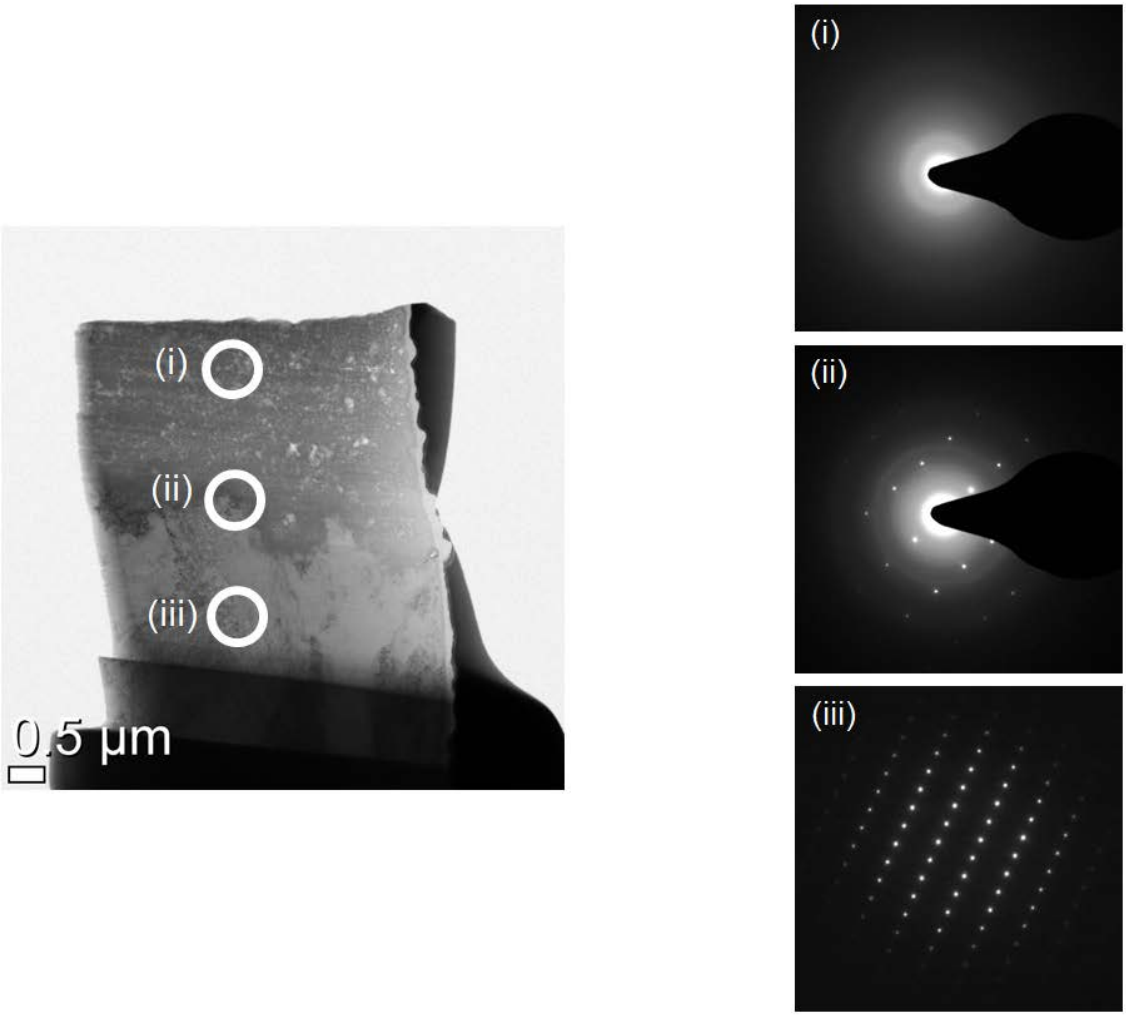

Fig. S5. Microstructural changes from degrading interface of Mg alloy implant.

Scanning TEM image of degrading interface of Mg alloy implant. (i) SAD pattern indicating amorphous Mg, O rich region. (ii) SAD pattern showing mixture of amorphous and crystalline structure at the interface between Mg, O rich region and Mg alloy region. (iii) SAD pattern of crystalline structure at Mg alloy region.

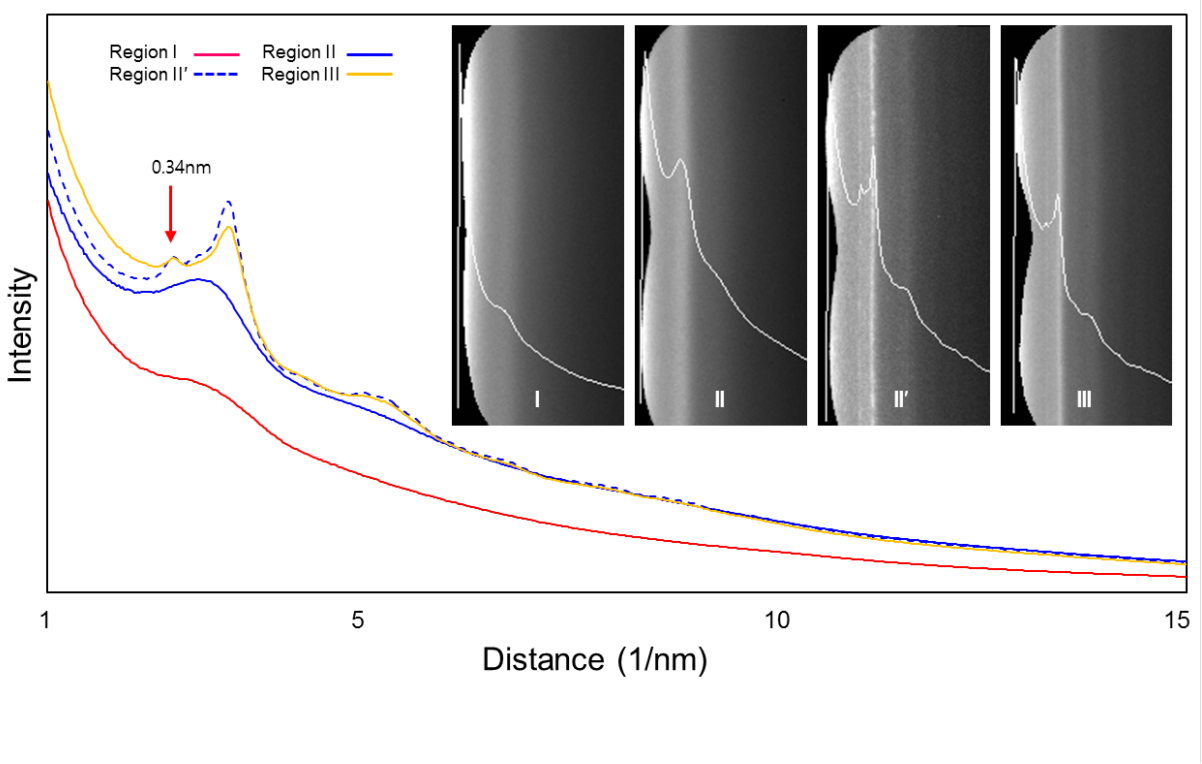

Fig. S6. Distance dependent crystallographic property (PASAD analysis) of interface from Mg alloy implant to bone region.

Region I (Mg, O-rich) and region II (Ca, P-rich) showed a typical amorphous pattern, whereas region II′ appeared to have crystallized pattern with lattice space of 0.34 nm in apatite (002) plane. Region III consisting bones showed crystalline pattern from typical (002) plane. At right upper side, the azimuthal projection images inserted profiles at each region were shown.

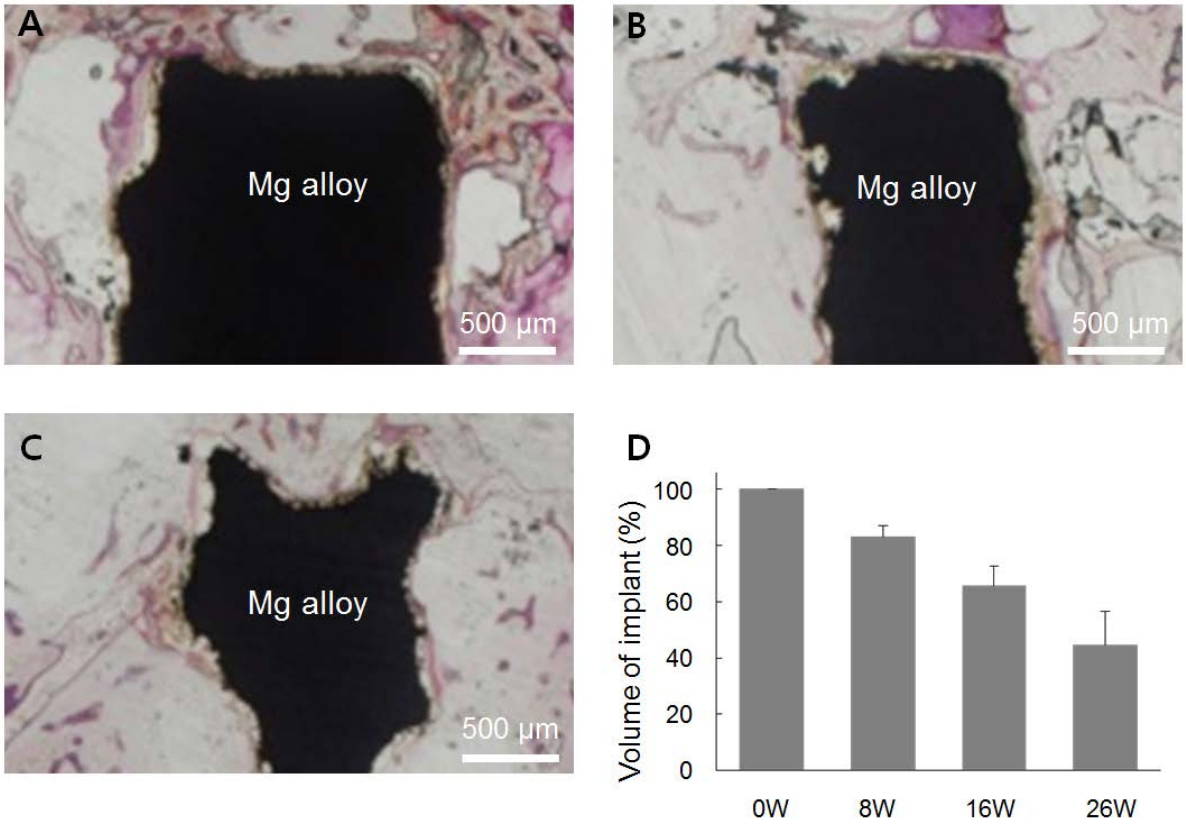

Fig. S7. Biodegradation of Mg alloy implant.

(A) 8 weeks postoperation of Mg alloy sample on femoral condyle of NZW rabbits, (B) 16 weeks postoperation, (C) 26 weeks postoperation, (D) Volume changes of implanted samples over 26 weeks measured with micro CT (N=10, Error bar shows means ±SD).

In order to measure the degradation rate using μCT, only the degraded Mg alloy was extracted by excluding surrounding bones. The volume of initial samples before implantation measured using μCT was 18.68±0.22 mm^3 (Theoretically, designed volume it should be 18.84 mm^3). After 8 weeks of implantation, 17.13% of the volume was degraded and the sample volume was reduced down to approximately, 15.48±0.84 mm^3. 34.74% of the initial volume was degraded after 16 weeks of implantation and the measured volume was 12.19±1.32 mm^3. It is an additional 17.61% volume degradation from the 8 weeks samples and the rate of degradation is very close to that of 8 weeks specimen. Samples from 24 weeks post-implantation showed larger standard deviation than samples from 8 and 16 weeks but the degradation trend was very similar. 21.19% additional volume was lost from the samples from 16 weeks and the measured volume was 8.23±2.27 mm^3. As shown in the figure below, the overall degradation behavior of the implant samples in vivo is quite stable.

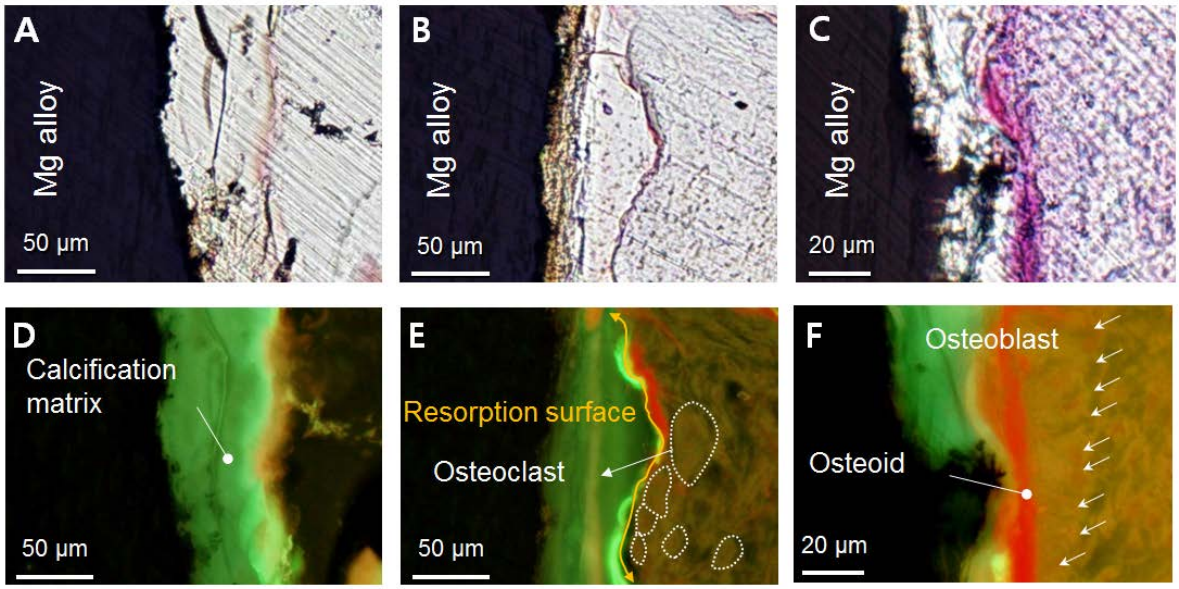

Fig. S8. Observation of remodeling initiation at Mg alloy interface using Villanueva stain. (A,D) Calcification matrix at the interface of degrading Mg alloy sample observed in natural and fluorescent light mode. (B,E) Observation of calcification matrix being absorbed by OC under natural and fluorescent light mode. (C,F) Observation of line formation by osteoid along the calcification matrix, which is followed by OB lining.

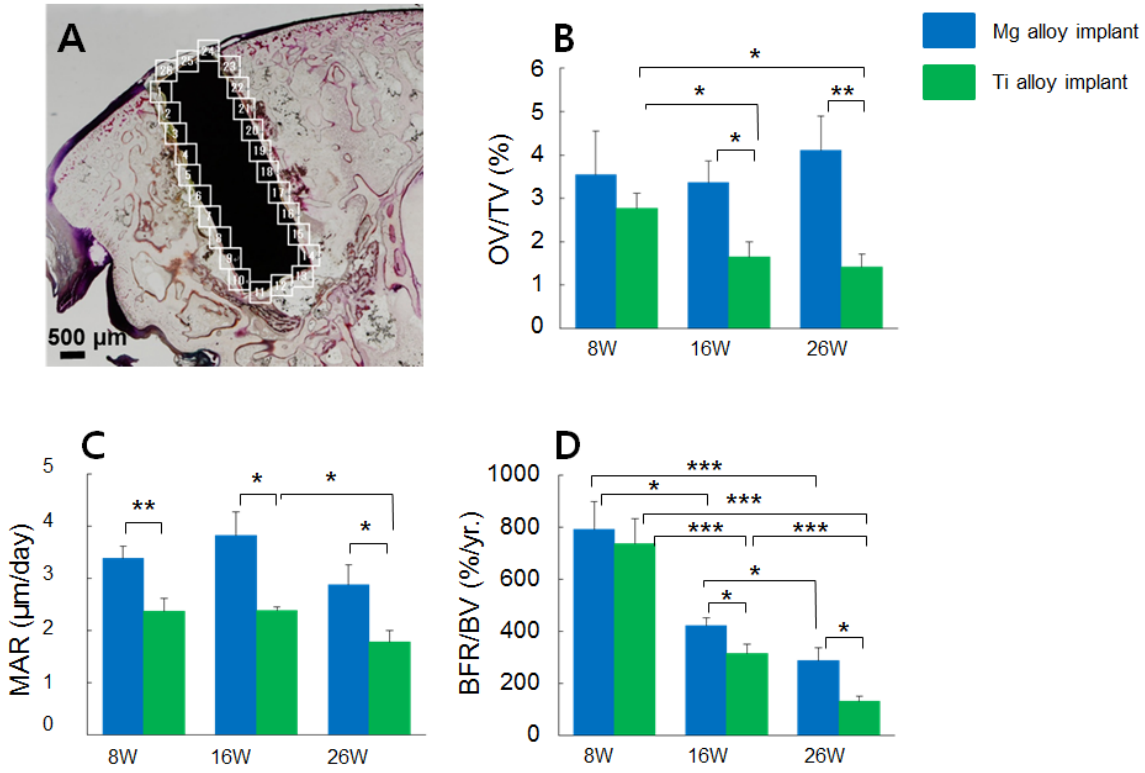

Fig. S9. Histomorphometrical analysis between biodegradable implant (Mg alloy) and conventional implant (Ti6Al4V alloy).

(A) 500 x 500 μm square areas were selected along the implant interface and analyzed statistically for each category. (B) Change of OV/TV (osteoid volume/tissue volume). (C) Change of mineral apposition rate (MAR). (D) Change of BFR/BV (bone formation rate/bone volume). N=5, *; P<0.5, **; P<0.01, ***; P<0.001.

Note) OV/TV is used as the primary parameter directly measured as an indicator of bone formation (2). MAR is used as a mineralization index calculated by dividing the distance between the edge of two consecutively labeled lines or midpoints by the time (3, 4). BFR/BV is the equivalent concept to bone turn-over rate, which is used as a mineralization index (3, 4).

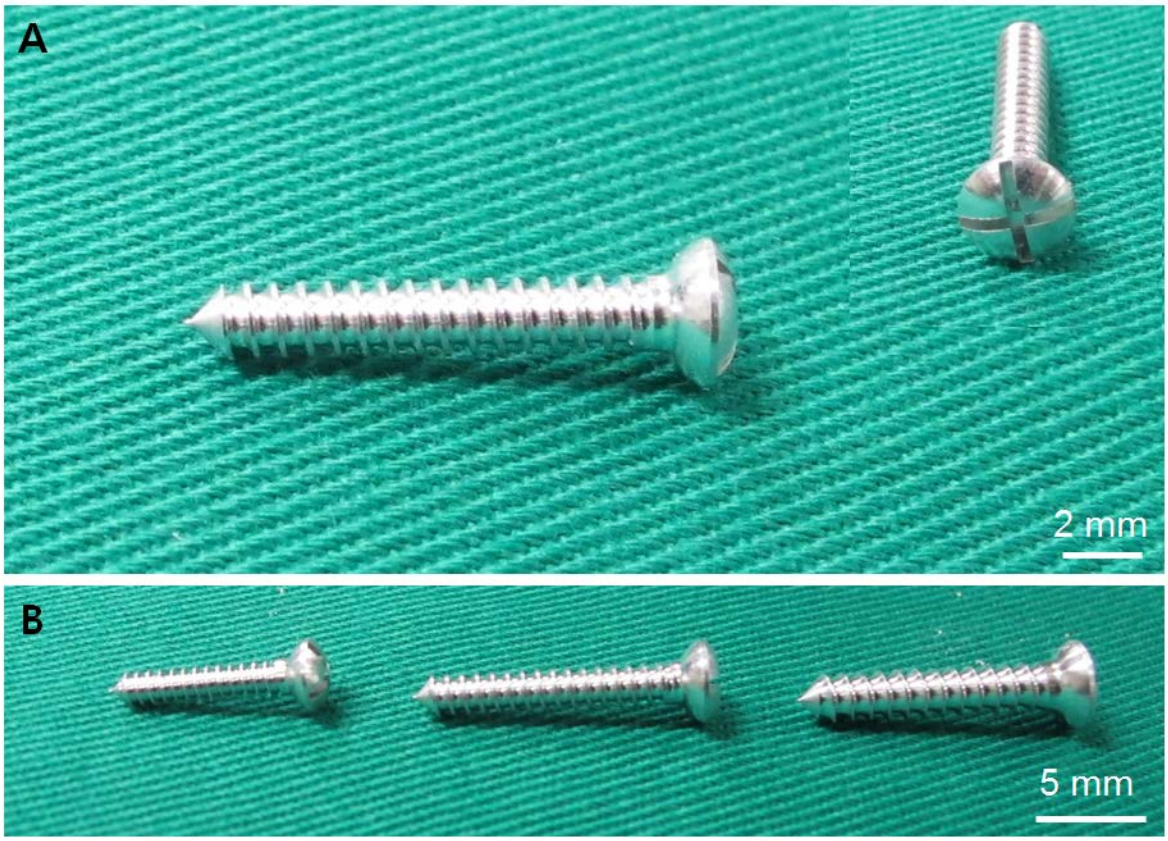

Fig. S10. Images of Mg alloy screws used in clinical trials.

(A) Images of Mg alloy implant screw (D 2.3mm x L 14mm). (B) Various sizes of Mg alloy screws used in the clinical study. From left, D 2.0mm x L 10mm, D 2.3mm x L 14mm, D 2.7mm x L 14mm.

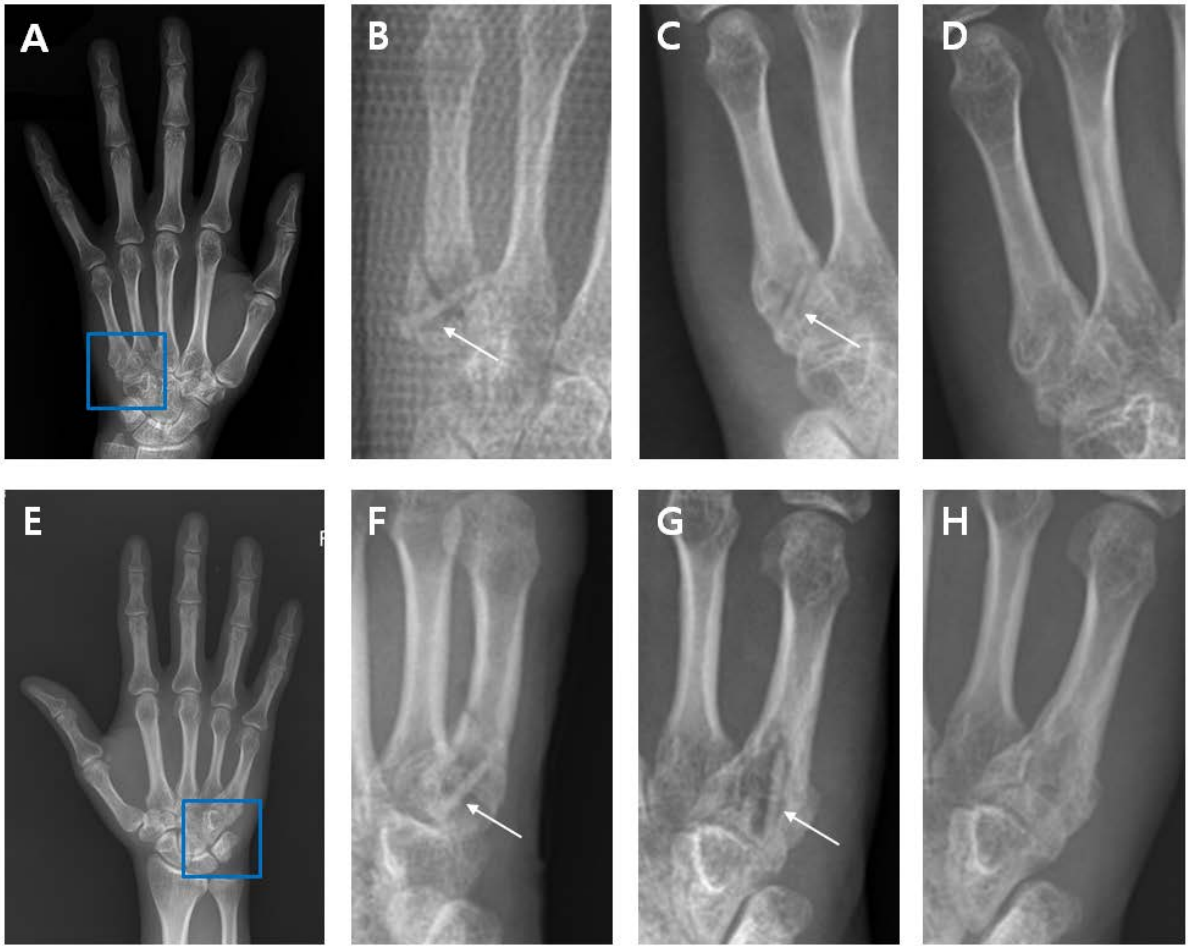

Fig. S11. 1-year follow-up of selected clinical trial cases.

(A) 29-year-old female patient with a fracture of the 5th metacarpal base of the left hand. (B) postoperative plain X-ray show a reduced intraarticular oblique fracture, fixed with a bioabsorbable metal cortical screw of D 2.3mm x L 14mm. (C) After 6 months the fracture is almost healed. The cortical continuity was complete and a faint fracture interface is shown. The diameter of the inserted bioabsorbable metal screw was reduced slightly and surrounding radioluscent area is observed. (D) At 1 year postoperation the fracture is completely healed and the bioabsorbable metal screw is absorbed and not found in plain X-ray. (E) 41-year-old male patient with a fracture of the 5th metacarpal base of the right hand. (F) postoperative plain X-ray show a reduced extra-articular transverse fracture, fixed with a bioabsorbable metal cortical screw of D 2.3mm x L 14mm. (G) After 6 months the fracture is almost healed.

The cortical continuity was almost complete and a faint fracture interface is shown. The diameter of the inserted bioabsorbable metal screw was reduced slightly and surrounding radioluscent area is observed. (H) After 12 months of surgery the fracture is completely healed and the bioabsorbable metal screw is absorbed and not shown in plain X-ray.

Fig. S12. Complete degradation of Mg alloy screw and bone healing of the proximal phalanx comminuted fracture over 1 year period.

(A) 20-year-old male patient with the 4th proximal phalanx comminuted fracture of the left hand. (B) Implantation site immediately taken after the surgical procedures to fix proximal phalanx comminuted fracture with Mg alloy implant (D 2.0 mm x L 10 mm) after 3 month. (C) Complete degradation and bone healing after 1-year postoperation. (D) Whole X-ray image of 1 year after implantation. White arrow shows the fracture site and implantation site.

Supplementary References

1. Han HS, et al. (2014) The evaluation of histological methods for biodegradable magnesium. *Eur Cell Mater* 28(Suppl. 3):83.

2. Koyama H, Nakade O, Takada Y, Kaku T, Lau KH (2002) Melatonin at pharmacologic doses increase bone mass by suppressing resorption through down-regulation of the RANKL-mediated osteoclast formation and activation. *JBMR* 17(7):1219-1229.

3. Hiramatsu R, et al. (2013) Occurrence of new bone-like tissue formation in uremic tumoral calcinosis. *Bone* 52(2):684-688.

4. Parfitt AM, et al. (1987) Bone histomorphometry: standardization of nomenclature, symbols, and units. Report of the ASBMR histomorphometry nomenclature committee. *JBMR* 2(6):595-610.